CHEMICAL PHYSICS

The physics of cement cohesion

Abhay Goyal[1]*†, Ivan Palaia[2,3†], Katerina Ioannidou[4,5,6], Franz-Josef Ulm[6], Henri van Damme[7], Roland J.-M. Pellenq[5,8], Emmanuel Trizac[2], Emanuela Del Gado[1]*

Cement is the most produced material in the world. A major player in greenhouse gas emissions, it is the main binding agent in concrete, providing a cohesive strength that rapidly increases during setting. Understanding how such cohesion emerges is a major obstacle to advances in cement science and technology. Here, we combine computational statistical mechanics and theory to demonstrate how cement cohesion arises from the organization of interlocked ions and water, progressively confined in nanoslits between charged surfaces of calcium-silicate-hydrates. Because of the water/ions interlocking, dielectric screening is drastically reduced and ionic correlations are proven notably stronger than previously thought, dictating the evolution of nanoscale interactions during cement hydration. By developing a quantitative analytical prediction of cement cohesion based on Coulombic forces, we reconcile a fundamental understanding of cement hydration with the fully atomistic description of the solid cement paste and open new paths for scientific design of construction materials.

INTRODUCTION

Concrete, made by mixing cement with water, sand, and rocks, is by far the most used man-made substance on earth. With a world population projected to grow past 9 billion by mid-century, there is need for more and better infrastructure (*1*), with no other material that can replace concrete to meet our needs for housing, shelter, or bridges. However, concrete, as it is now, is not sustainable since cement production alone is responsible for substantial amounts of man-made greenhouse gases. While even a slight reduction of its carbon footprint will markedly reduce global anthropogenic CO_2 emissions, meeting emission reduction targets for new constructions calls for deeper scientific understanding of cement properties and performance (*2*).

The dissolution of cement grains in water and reprecipitation of various hydration products, with calcium-silicate-hydrates (C-S-H) being the most important (*3*, *4*), drive the setting of cement into a progressively harder solid that binds together concrete and determines its mechanics (*5*). During this process, strongly cohesive forces develop from the accumulation and confinement of ions in solution between the surfaces of C-S-H, whose surface charge progressively increases over time (*6*–*8*).

Net attractive interactions between equally charged surfaces in ionic solutions are common in colloidal materials or biological systems (*9*–*15*). The comprehensive analytical theory developed nearly a century ago by Derjaguin, Landau, Verwey, and Overbeek (DLVO), which relies on a mean-field approximation treating the ions as an uncorrelated continuum, captures some of these cases (*9*). For cement hydration products such as C-S-H, however, the DLVO description is inapplicable since the ions in solution are mostly multivalent (such as Ca^{2+}) and confined between surfaces whose surface charge density rapidly reaches values up to $\simeq 3$ to $5e^-/nm^2$ in the layers of hardened C-S-H (*4*, *8*, *16*). Sure enough, DLVO theory does not predict any cohesion for cement (*7*, *8*).

Monte Carlo simulations of a primitive model (PM) for ion confinement, instead, have proven that ions, confined in water between charged surfaces, can induce net attractive forces for a range of surface charge densities relevant to C-S-H (*6*, *17*, *18*) because of the correlations that stem from the discrete nature of ions. Nevertheless, these PM studies predict cohesive strengths at most of $\simeq$60 MPa, in clear contradiction with experiments and with the fully atomistic understanding of hardened C-S-H achieved over the past 10 years (*4*, *8*, *19*–*21*). The cohesive strength of hardened cement is 100 times larger than that, and the presence of water is limited to a few molecules per ion, whereas it is treated as a bulk dielectric continuum in the PM approach. There is therefore a knowledge gap in the fundamental understanding of how nanoscale cohesive forces emerge during cement hydration, as different chemical reactions drive the increase of the surface charge of cement hydrates and the ion confinement (*22*).

We now fill this gap with three-dimensional (3D) numerical simulations that feature a simple but molecular description of ions and water, providing a quantitative picture of how cement cohesion develops during hydration. When one considers explicitly the role of water, it becomes clear how its capability to restructure and reorient around the ions drives the optimized organization of interlocked ion-water structures that determine the net cohesive forces and their evolution.

As ion confinement and surface charge density increase, with markedly weakened water dielectric screening, electrostatic forces and discreteness effects are markedly amplified and glue together the ion-water-surface assembly into a highly cohesive state. While we quantitatively recover several key experimental findings in real cement (*23*–*28*) and the main features of the fully atomistic description of hardened C-S-H (*16*, *29*), we test the emerging physical picture against an analytical theory that distills the essential ingredients of the net interactions beyond the traditional PM assumptions, for

[1]Department of Physics, Institute for Soft Matter Synthesis and Metrology, Georgetown University, Washington, DC 20057, USA. [2]Université Paris-Saclay, CNRS, LPTMS, 91405 Orsay, France. [3]Department of Physics and Astronomy, University College London, London WC1E 6BT, UK. [4]Laboratoire de Mécanique et Génie Civil, CNRS, Université de Montpellier, 34090 Montpellier, France. [5]Massachusetts Institute of Technology/CNRS/Aix-Marseille University Joint Laboratory, Cambridge, MA 02139, USA. [6]Department of Civil and Environmental Engineering, Massachusetts Institute of Technology, Cambridge, MA 02139, USA. [7]École Supérieure de Physique et Chimie Industrielle de la Ville de Paris, 10 rue Vauquelin, 75005 Paris, France. [8]Department of Physics, Georgetown University, Washington, DC 20057, USA.
*Corresponding author. Email: ag1473@georgetown.edu (A.G.); ed610@georgetown.edu (E.D.G.)
†These authors contributed equally to this work.

a range of materials and systems in similar strong electrostatic coupling conditions.

RESULTS

The intricacy of chemical reactions during cement hydration and setting makes it hard to identify the fundamental physical mechanisms that control cement cohesion. C-S-H is a nonstoichiometric compound, with structure and composition variability, even more pronounced at the earlier stages of the hydration (*4*, *21*, *30*, *31*). The charged surfaces of C-S-H nanoparticles confine ions and water in nanometer-sized pores (*18*, *32*), and studies of titration of the surface silanol groups indicate that during early hydration, as a result of the changing solution chemistry, the surface charge of C-S-H increases with increasing pH, coupled to the combined precipitation of calcium hydroxide (*31*). Experimental and simulation efforts over the past decade have clarified the atomistic details of the final hardened C-S-H, in terms of atomic pair distribution functions, composition variability, and even cohesive strength (*4*, *20*, *21*, *23*, *24*). However, a direct link between the surface charge and chemistry, the emerging nanoscale cohesion, and the final material properties is missing.

To address this question, we have used a semi-atomistic computational approach, in which ions and water are represented explicitly while the C-S-H surface properties at different hydration stages are recapitulated through surface charge densities σ from 1 to $3e^-/nm^2$. C-S-H is often characterized in terms of Ca/Si ratios, and with pH values typical of cement hydration, the range of surface charge densities considered here approximately correspond to the relevant range of Ca/Si ratios between 1 and 2 (*16*, *30*, *33*). Representing C-S-H surfaces with smooth, uniformly charged walls is clearly a simplification since their strongly heterogeneous nature is known (*21*), but it is essential to the extended spatiotemporal analysis performed here. Thanks to this simplification, we can extensively sample ion and water structure and dynamics in molecular dynamics (MD) and grand canonical Monte Carlo (GCMC) simulations and extract the net pressure that ions and water induce between the confining C-S-H charged surfaces.

In our 3D study, C-S-H surfaces are planar (walls), consistent with the platelet-like morphology of the nanoparticles (*30*, *32*, *34*), and the ions confined in between them, neutralizing the surface charge, are calcium (Ca^{2+}). To a reasonable approximation, this represents the most relevant portion of the ions confined between C-S-H surfaces during cement hydration (*6*, *8*, *16*). The walls have periodic boundaries along *x* and *y* and are separated by a distance *D* along the *z* direction. For (Ca^{2+}) and C-S-H surfaces, we include both short-range steric/dispersion and long-range electrostatic forces, as described in Methods. Explicitly including the molecular degrees of freedom of water (we use SPC/E and, in some cases, TIP4P/2005 water, as also described in Methods) is key to capture its behavior under confinement (*35*–*37*).

Already for the lowest σ = $1e^-/nm^2$, corresponding to very early hydration, the inclusion of explicit water leads to a net attraction (Fig. 1A) arising from strong and long-ranged correlations in ion positions: The ions are localized in the *z* direction like in the PM, but with explicit water, the pair correlation of their positions *g*(*r*) in the *xy* plane has clear peaks that persist to large distances (Fig. 1B). The same *g*(*r*) for PM (bare ions) indicates instead a spatial arrangement close to uncorrelated, and a simplistic attempt to account for the ions' hydration shells by considering a larger effective ion size is still insufficient to capture the long-range effect of water and the related pressure profile.

In the confined space between charged surfaces, the ion hydration shells may differ significantly from those in bulk water. In general, we identify the ion-water structures as *n*-mers, *n* being the number of water molecules surrounding an ion (see Methods), as in Fig. 1C. At relatively large separations of $D > 20$ Å, hydration shells have typically eight water molecules as in bulk water (Fig. 1C), consistent with a range of simulations and experiments (*38*, *39*). Computing dynamic correlations such as those measured through quasi-elastic neutron scattering (QENS) reveals relaxation times consistent with experimental values (*38*, *39*): Hydration shells are energetically favored because of the high hydration energy of Ca ions (*40*) but quite dynamical as individual water molecules switch between free and bound states (see section S1).

As *D* is decreased, a larger fraction of the total water is in the hydration shells, while ions become increasingly correlated [see the strongly pronounced peaks in the *g*(*r*) in Fig. 1B]. Further confinement, however, starts to markedly affect the hydration shells: By $D = 8$ Å, the surfaces are squeezing the ions into a single layer and pressing against their hydration shells (Fig. 1D), eventually reduced to ≃5 water molecules per ion. Hence, reducing *D* from 9 Å (where the full 8-mer hydration shell can be accommodated) to 7 Å (where this is not possible anymore) requires overcoming an energy barrier. The calcium ion hydration enthalpy of ≃−640 k_BT (or −1600 kJ/mol) (*40*) indicates that a cost of ≃240 k_BT is required to reduce a typical hydration shell of eight water molecules to one with five water molecules, leading us to estimate that a pressure change of roughly ≃1.25 GPa would be needed. Our rough calculation obviously overestimates the energetic contribution, which for the first water molecule in a hydration shell is larger than for the eighth, because of steric repulsion, dipole-dipole interactions, and entropic costs. Numerical studies and x-ray diffraction, which instead consider only the contribution of water molecules in the first shell to the hydration free energy, provide a lower bound of ≃0.67 GPa to the energy cost for reducing the calcium hydration shell (*39*). The pressure that we measure (Fig. 1A) indeed features a nonmonotonic dependence on *D*, and the magnitude of the ≃1 GPa jump in pressure between $D = 9$ and 8 Å is well consistent with our estimated range. This shows that the high stability of the hydration shells can give rise to a competing intermediate-range repulsion (*41*, *42*), confirming early atomic force microscopy measurements on cement hydrates (*7*) and consistent with gel morphologies obtained in C-S-H coarse-grained simulations and seen in microscopy imaging (*43*–*45*). The finite stability of the bulk-like hydrated structures in increasing confinement provides a fundamental mechanism for this nonmonotonic dependence of the nanoscale forces on surface separation, fairly robust to the presence of salt and other ions.

At σ = 2 and $3e^-/nm^2$ (later hydration stages), the ions are increasingly localized in the *z* direction and squeezed with their hydration shells against the walls [see ion density profiles in Fig. 2 (A and B)], becoming unable to maintain full hydration shells in favor of smaller, hemispherical ones. The effect of confinement constraints are very clear at σ = $2e^-/nm^2$ and $D = 20$ Å, where the ion profiles show double peaks, split between ions with two distinct types of hydration shells (Fig. 2C). With further confinement ($D = 8$ Å), all ions are squeezed against the walls and there is no splitting of the ion density peaks. Last, for the highest surface charge σ = $3e^-/nm^2$, the ions stay pressed against the walls even at large separations.

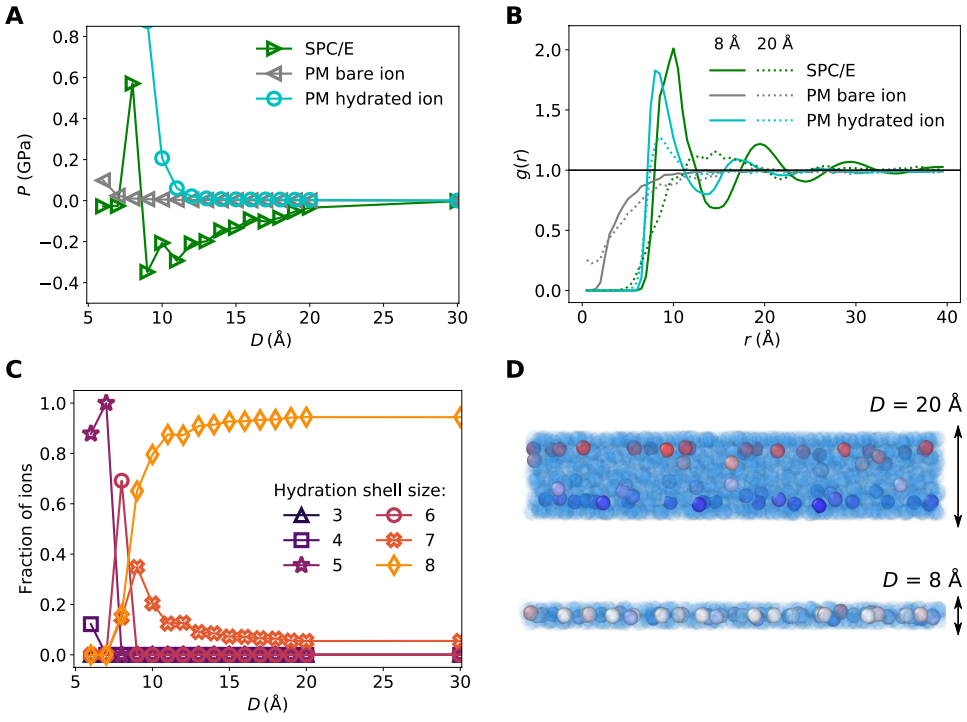

Fig. 1. Results from simulations with PM and SPC/E water at $\sigma = 1e^-/nm^2$. Here and in subsequent figures, all data are averaged over 10^6 MD steps after having reached equilibrium. Error bars are smaller than the symbol sizes. In (**A**), we show the net pressure between the C-S-H surfaces. With explicit water, we obtain negative pressures, i.e., net attraction, that cannot be found with the PM approach, even considering an increased effective ion size due to hydration. This stems from much stronger ion-ion correlations seen in (**B**), where we plot the ion pair correlation in the *xy* plane at $D = 8$ Å and $D = 20$ Å. Using the hydrated ion size in the PM creates a first peak that is similar to what we get with explicit water, but it cannot replicate the long-ranged correlations. The water behavior is more complex than that and strongly depends on confinement. Looking at the hydration shell size (**C**) at large separation, we observe nearly full hydration shells of seven to eight water molecules. As *D* is decreased, the shell size does not immediately change and the shells make up a larger portion of the water, which affects its ability to screen electrostatic interactions. When confined to $D = 8$ Å, the ions coalesce into a single layer (**D**) and the shells are pressed against the walls, resulting in a barrier to overcome.

With ions localized sufficiently close to the wall, two layers can be accommodated even for the strongest confinement, but the hydration shells are significantly modified by the confining surfaces and are hemispherical for all separations.

At high confinement ($D = 8$ Å), the ions in the two layers have distinct but strongly coupled ordering. With layers being defined by the ion position z_i, the ion pair correlation $g(r)$ can be separated into intra- and interlayer contributions, considering ions in the same (intra) or opposite (inter) layers (Fig. 3A). Despite the separation in *z*, the *xy* positions remain strongly correlated and, at high σ, form a staggered square lattice: The ground-state configuration predicted for confined charges in a strong electrostatic coupling regime (defined by high-enough surface charge density and strongly confined ions) where ion-ion interactions are included (*46*). The distance corresponding to the first peak of the $g(r)$ decreases with increasing σ, and for $\sigma = 3e^-/nm^2$, it is in good agreement with that of the Ca-Ca $g(r)$ recently obtained with x-ray scattering in C-S-H (*23*, *24*), considering the effect of surface heterogeneities and the surface charge density variation in the real material.

The increase in spatial correlations is associated to strongly correlated dynamics and localization of the ions. The ion intermediate scattering function computed for $q_z = 5.65$ Å^{-1} (roughly corresponding to the peak width of the ion density profiles at the highest σ) is plotted as a function of time *t* in Fig. 3B, whereas data for a range of q_z values are provided in section S1. Increasing confinement and surface charge density clearly enhances the dynamical correlations and ion localization, with the effect being particularly marked at the highest surface charge. The decrease in mobility and increase in correlation strength that we see with σ is coupled to a massive increase (in absolute value) in the net attractive pressure between the two C-S-H surfaces. At $\sigma = 3e^-/nm^2$, the pressure minimum is $P_{min} \simeq -6$ GPa (Fig. 3C), consistent with atomistic simulations and experiments (*4*, *19*, *21*, *29*).

To further understand the dependence of the pressure, we note that the level of confinement changes the water arrangement around ions (Fig. 4A), and for $\sigma = 3e^-/nm^2$, we reach a balance of 5- and 6-mers beyond $D \simeq 15$ Å, whereas at even smaller *D*, the surface limits both the number of water molecules and the space available around the ions, leading to a prevalence of 3- or 4-mers at the smallest separation $D = 6$ Å (Fig. 4B).

Let us now consider that water molecules consist of a spherical particle endowed with a dipole moment, an approach that removes one rotational degree of freedom per water molecule relative to the SPC/E (or TIP4P/2005) water models but allows us to estimate analytically the minimum free energy configurations for the *n*-mers. With this assumption, the energetic gain when a dipole adsorbs to an ion (neglecting any other effect) is $\simeq 64\ k_BT$ per water molecule (shown by the turquoise line in Fig. 4C). We can include dipole-dipole interactions within *n*-mers (squares) and then interactions with other hemispherical *n*-mers (circles) to observe that the energetic gain

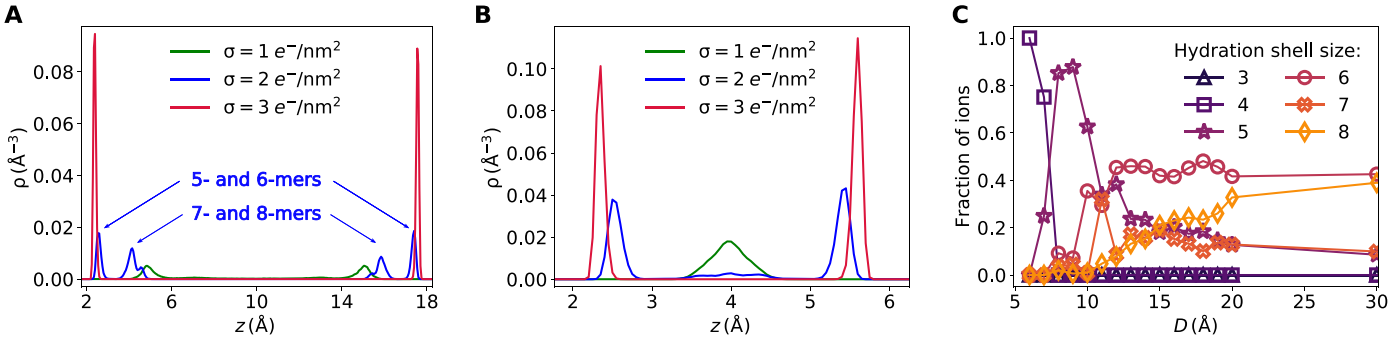

Fig. 2. Ion density profiles and ion hydration shells. Plots of ion density profiles at (**A**) $D = 20$ Å and (**B**) $D = 8$ Å. By increasing surface charge density, we see an increasing localization of ions in the z direction. For $\sigma = 2e^-/\text{nm}^2$ at large D (**C**), there is a split between wall ions with a hemispherical hydration shell of five to six water molecules and shifted ions with a nearly full hydration shell of seven to eight water molecules. At lower D or higher σ, the shifted ions are suppressed and all ions are close to the wall, in stark contrast to the situation at $\sigma = 1e^-/\text{nm}^2$ and $D = 8$ Å where all the ions coalesce into a single layer.

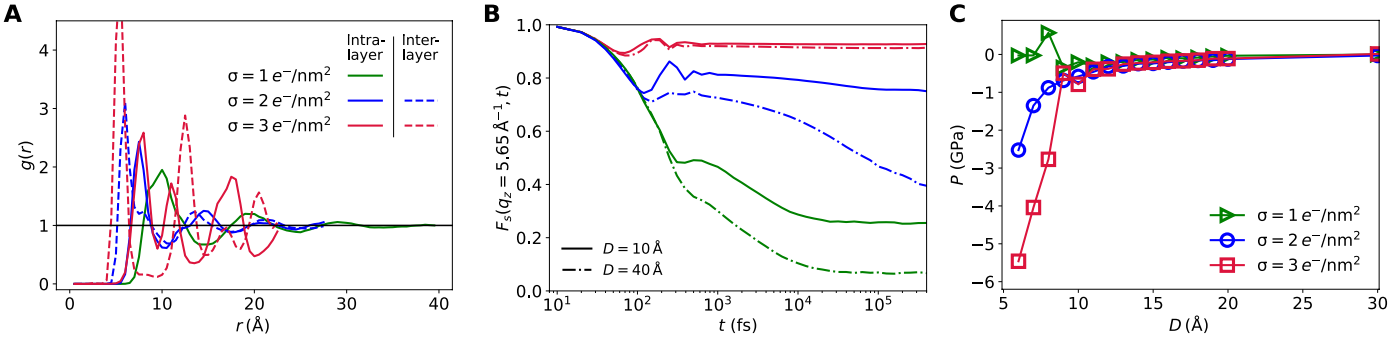

Fig. 3. Spatiotemporal correlations for different surface charge densities. (**A**) The xy pair correlation $g(r)$ between ions shows that, as σ increases at fixed separation $D = 8$ Å, ions become closer together and their positions become more correlated. For $\sigma = 1e^-/\text{nm}^2$, the ions are in a single layer equidistant from the confining walls, but at higher σ, there are two layers, one near each wall. For those, we split the $g(r)$ into the components corresponding to correlations within and between layers, demonstrating a clear spatial organization despite the separation in z. (**B**) Intermediate scattering functions $F_s(q_z, t)$ for the ions measured for the same σ values as in (A) and for two different surface separations D. The data demonstrate that the stronger spatial correlations with increasing surface charge density in (A) correspond to increasingly correlated dynamics and more strongly localized ions. (**C**) The increasing correlations drive the overall pressure between the confining walls to become increasingly attractive, reaching $P_{\text{min}} \simeq -6$ GPa at $\sigma = 3e^-/\text{nm}^2$.

decreases with increasing n but is still more than an order of magnitude higher than k_BT when going to $n = 6$. The minimum energy configurations used in the calculations are sketched in Fig. 4C and correspond to the shapes observed in simulations for the higher surface charge densities. Taking into account the reduction of water entropy due to the confinement of the molecule and its dipole on the ion and, therefore, including finite temperature in our (so-far) ground-state calculations, one obtains that 5- and 6-mers have the same free energy of formation, within a tolerance $\simeq k_BT$ (see section S2.1). This explains the right part of Fig. 4B, where these two structures appear in commensurate proportions.

The large energetic gain for forming these n-mers suggests that they are stable objects, and this is exactly what is observed in the simulations where their lifetimes are found to be longer than the simulation time. By computing the dynamics of the water, we determine that, at the high surface charges where these hemispherical n-mers exist, there is now a clear distinction in the behavior of water that is bound in n-mers and free water (Fig. 4D, continuous lines), different from what happens at low surface charge density (dashed lines). QENS, differential scanning calorimetry, and nuclear magnetic resonance experiments on cement hydrates indeed provide evidence of distinct populations of unbound and physically bound water molecules emerging during cement hydration (*25*–*28*). The experimental observation of a bound water fraction increasing with hydration time in cement is perfectly captured here by the dynamical signature of physically bound water at high σ (Fig. 4D) and by the increase in its amount with confinement (Fig. 4E).

The effect of confinement can be simply understood by considering that the free energy gained when a water molecule is adsorbed on a 3-mer to form a 4-mer, or on a 4-mer to form a 5-mer, is energy dominated and amounts to negative several tens of k_BT: It is always extremely favorable to adsorb water molecules on ions from the bulk to increase n, at least up to $n = 5$. As a consequence, upon increasing the confinement, i.e., when progressively fewer water molecules are available in the nanoslit, all of them are adsorbed on ions. This observation allows us to predict the expected fraction of adsorbed water (Fig. 4E) and the peaks of the n-mer distribution (fig. S6) for $n = 3$, 4, and 5 by assuming that all available water is bound in n-mers. Using different water models (both SPC/E and TIP4P/2005) does not significantly change these outcomes

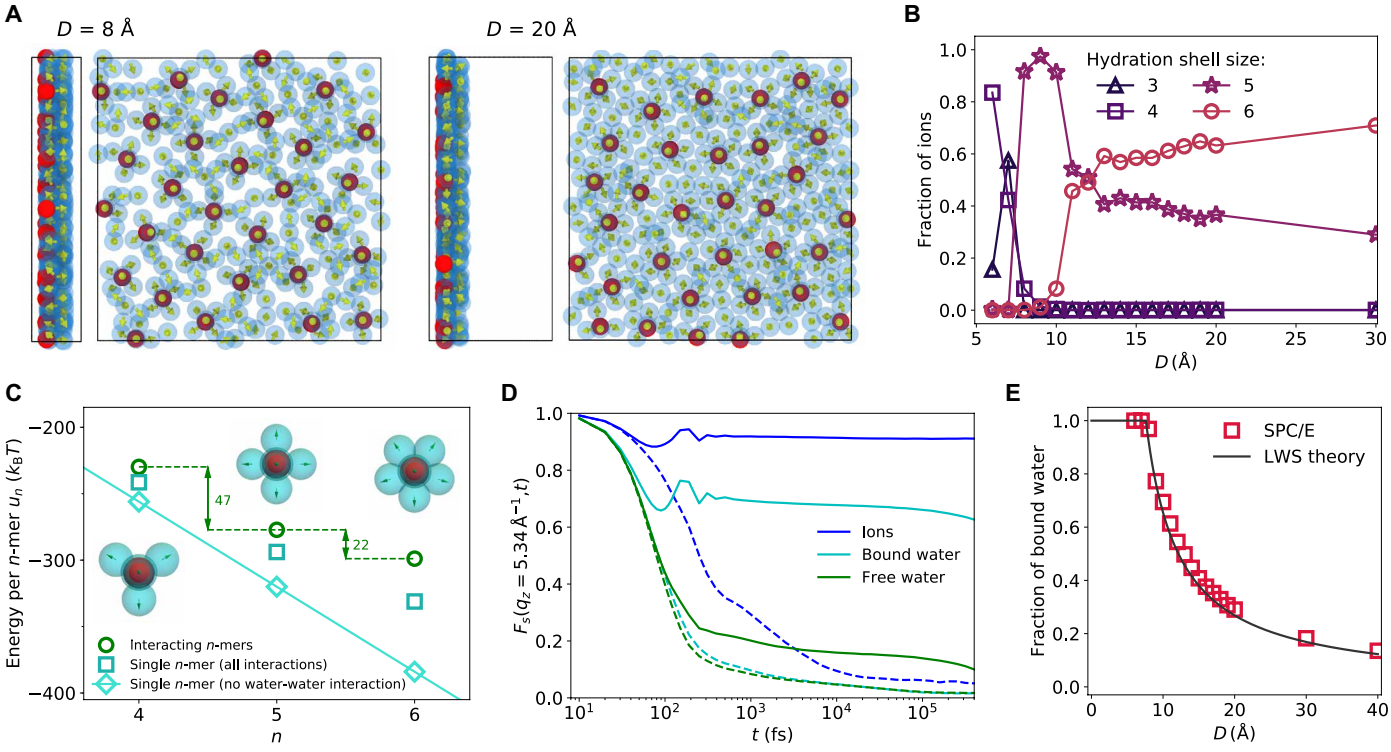

Fig. 4. *n*-mers and bound water. (**A**) Simulation snapshots and ion-water coordination as a function of surface separation (side and front views). The snapshots show the formation of *n*-mers with an ion and its *n* water hydration shell. (**B**) A transition from 3-mers at low separation to a balance of 5- and 6-mers at larger separations is observed. (**C**) Ground-state energy calculations reveal that there is a large gain for a dipole to adsorb on an ion, explaining the formation of these effective objects. As *n* grows larger (to 5 or 6), the additional entropic cost becomes sufficient to offset that energetic gain, with a 6-mer being the largest possible semihemispherical object. (**D**) Intermediate scattering functions for ions and bound and free water at $D = 20$ Å for $\sigma = 3e^-/\text{nm}^2$ (continuous lines) and $\sigma = 1e^-/\text{nm}^2$ (dashed lines). The data show the enhancement of the ion localization and the clear distinction between bound and free water at high surface charge. (**E**) The fraction of water in *n*-mers as a function of separation. At small *D*, almost all water is bound up in these *n*-mers, with *n* limited by water availability. At larger separations, the balance of energetic gain and entropic cost limits *n*-mer size (see Methods and section S2.1). These theoretical arguments enable quantitative predictions about the water structure, via a novel approach based on locked water shells (LWSs), which agree with simulations.

(see section S3.1). These findings are also in excellent agreement with fully atomistic simulations of hardened C-S-H (i.e., corresponding to the end of the hydration process), where Ca ions are typically associated only to three to four water molecules (*4*).

It had already been speculated that, because there are few water molecules in the interlayers of the hardened C-S-H, the effect of the dielectric properties of water (a fundamental ingredient of PM) on the cohesion should have been significantly reduced (*8*). We find that the *n*-mers act as stable effective objects and interact in a completely water-depleted environment. The water permittivity tensor ε_r is anisotropic (see section S3.2), indicating that water dielectric properties cannot generally be recapitulated in a simple constant. Nonetheless, with decreasing *D*, the components of ε_r rapidly approach 1, compared to bulk water permittivity of ≃78, in line with recent works in other contexts (*35*, *37*) or atomistic simulations of C-S-H (*16*).

To ultimately test this picture and distill its essential ingredients, we develop an analytical theory for the pressure profile beyond DLVO, taking advantage of the existence of "correlation holes" around each ion (*14*). The idea is to account for ion-ion correlations by defining a region around each ion in which other ions are prohibited from entering. This is confirmed by the fact that the pair correlation functions $g(r)$ in Figs. 1 and 3 exhibit strongly depleted short-scale features, with $g \simeq 0$. Using this concept, we compute the local effective field κ felt by an *n*-mer due to the presence of all other *n*-mers in a staggered arrangement (see Methods and section S2.2). This can be used to calculate the ion density profiles, which match the profiles obtained in simulations, as shown in Fig. 5 (A and B) [here, we have used only the dipolar interactions for the water to simplify the comparison to the theory, but qualitatively, the same behavior is shown in Fig. 2 (A and B)]. While the theory slightly overestimates the density peak heights, this still demonstrates how effective the *n*-mer–based theory is at predicting the microscopic details of the simulations. The interactions between *n*-mers and walls yield the pressure between the two surfaces. The Coulombic contribution is given by an analytical pressure equation, which is particularly simple (Eq. 8). Supplemented with the steric contribution (that becomes relevant only for $D < 6$ Å), this yields a total pressure in remarkable agreement with the simulations (see Fig. 5C).

The fact that our simulation data in the strong coupling regime are so well described by the analytical theory indicates that the underlying ground state is quite resistant to perturbations because the high surface charge and electrostatic cohesion dominate the overall behavior of the system. When we also consider the relatively good agreement with several aspects of full atomistic simulations and experiments where surface heterogeneities are naturally present, these findings suggest that our simplifying assumption of smooth planar

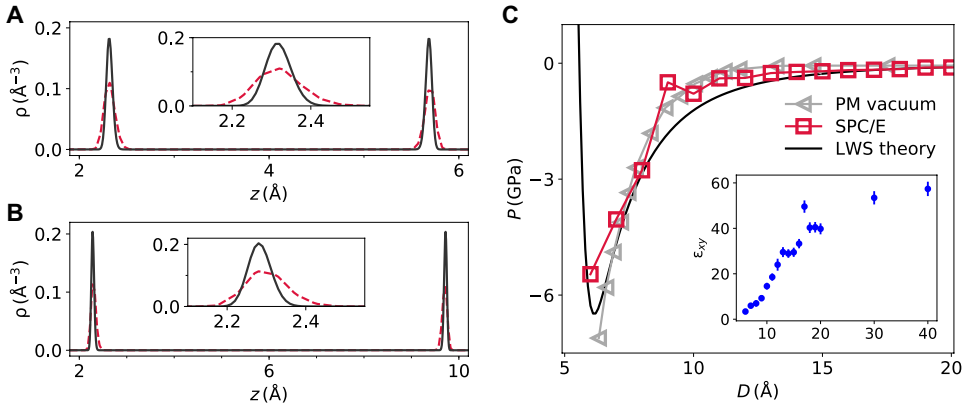

Fig. 5. Water dielectric screening and theoretical predictions of pressure. Ion densities can be computed through the theory of strong coupling and correlation holes, considering an *n*-mer as an effective ion and treating appropriately the Lennard-Jones interactions between the wall and *n*-mers. These computed density profiles (solid lines) are compared to the simulated profiles (dashed lines) for (**A**) $D = 8$ Å and (**B**) $D = 12$ Å. For this quantitative assessment, we compare with simulations that use a dipolar water model to more closely match the analytical calculations. While the theory predicts a somewhat sharper density peak, there is good agreement between the two. (**C**) From density profiles, one can compute the equation of state through a generalized version of the contact theorem (see section S2.2). This gives a calculated interaction pressure much stronger than earlier theories for implicit water models and close to what is seen in simulations. Because of adsorption of water into *n*-mers at small distances, the effective pressure in the explicit water simulations approaches what one would get for ions in vacuum, for which the rise of pressure at distances below six is not visible, since the Lennard-Jones contribution has been discarded for the sake of the argument. The inset shows how the in-plane component of the dielectric tensor is significantly reduced under confinement, consistent with previous studies (*16*, *35*, *37*) and explaining why water-free results are in unexpectedly good agreement with the full explicit water simulations.

surfaces may be sufficient, in this regime, to capture the overall behavior of the system. This is consistent with the fact that, in strongly correlated systems, the average inter-ion separation expressed by the $g(r)$ is fixed by electroneutrality. As a consequence, in the real material, the same mechanisms revealed here will remain at play, while absolute values of the net cohesive strength will also depend on surface charge density variation, additional surface heterogeneities, and the presence of other ionic species.

While, in our approach, water molecules are explicitly accounted for, they are all "captured" by ions, justified by the water dynamics at high confinement (section S1) and the consequential reduction in dielectric screening (Fig. 5C, inset). As a consequence, the typical interaction energies of the system get multiplied by a factor 78, leading to the marked increase in the cohesive strength. Ultimately, the effect of the water in terms of dielectric screening is much less important than in bulk conditions, to such an extent that water presence may be ignored altogether. This "locked water shell" (LWS) picture is well illustrated in Fig. 5C, showing that the results of simulations with explicit water and from the theory are close to those of PM simulations with a vacuum dielectric constant. The water-ion structuring is a complex function of confinement, surface charge density, and ion species/concentration. However, we can capture the leading effects of the strong electrostatic coupling by the "locked water" view, demonstrating that the net cohesion is due to the ion-water interlocking.

DISCUSSION

About one century after the early studies of cement hydration, the properties of C-S-H are still a matter of strong debate. Extensive studies, novel techniques, enhanced characterization, and imaging capabilities have greatly improved the knowledge of this complex material, ultimately returning a picture of variability of chemical composition, structural organization, and mesoscale morphology. Evidence of this variability has become increasingly clear and is obtained from many sources (*47*), with a net increase of data and information available. What is needed, at this point, is to identify the origin of such variability and understand its implications for material performance, durability, and sustainability.

Our results open the way to do just that. During cement hydration, as C-S-H continuously precipitates, ions and water get progressively confined between increasingly charged surfaces of cement hydrates. We have shown that these two factors, together, change ion-water interlocked structures and their stability, which, in turn, change the net pressure between C-S-H surfaces as hydration proceeds. Our semi-atomistic approach, by including surface charge and ion specificity, captures essential features of cement hydrates detected in experiments, from the ion arrangements to water population and dynamics to material strength. While it can be extended to include different counterions and mixtures in future studies, here, it has provided unique insight into how varying chemical composition that sets the surface charge density changes the water-ion structuring under confinement and, hence, strength and shape of the net interactions between cement hydrate nanoparticles. Understanding the origin and the evolution of cement cohesion in terms of fundamental components and mechanisms is key to identifying scientifically guided strategies, such as modifying the ionic composition and increasing cement strength to do more with less, to reduce the greenhouse gas emissions from cement manufacturing.

At the nanoscale, the variability of the structural organization of C-S-H in terms of different interlayer separations (*21*, *30*) can now be understood via the dependence of the interaction strength, and hence of the energy gain corresponding to different interlayer distances, on the degree of confinement. However, the evolving shape of the net interactions also has implications for larger length scales because it determines the anisotropic growth of cement hydrates aggregated into fibrils, lamellae, and layered mesophases that can self-assemble as C-S-H precipitation proceeds (*5*, *43*). It therefore provides the missing link from the nanoscale to the mesoscale aggregation kinetics and morphological variability of cement hydrates

(*19*, *21*, *23*, *24*, *30*, *45*–*49*). By the end of hydration, C-S-H becomes denser and denser, and its nanoscale features (including the interlayer distances and chemical compositions usually described in terms of Ca/Si ratio) play a predominant role in most observations and studies (*16*, *21*, *29*). Nevertheless, the earlier-stage mesoscale morphology controls the development of larger pores and contributes to local stresses in the initial gel network, which have consequences for the long-term evolution of the material and its interactions with the environment (*5*, *43*, *44*, *50*–*53*). The change in shape of the nanoscale interactions, with competing attraction and repulsion and a notable increase of the attraction strength with surface charge density during hydration, largely controls the morphology of the mesoscale structures that build the gel network and can markedly steer compressive or tensile stresses as the material progressively densifies and solidifies. These insights shed new light into the physics of cement setting and open new opportunities for scientifically grounded strategies of material design.

The fundamental understanding of the nature of the electrostatic coupling and the role of ion-water structures has implications beyond cement: A wide range of systems, including biological membranes, soils, and energy storage materials (*11*, *12*, *42*, *54*, *55*), feature aqueous ionic solutions with both strong Coulombic and confinement effects. While theories such as DLVO work with continuum approaches, we have seen that two discreteness effects interfere with mutual reinforcement: ionic correlation and dielectric destructuring. This calls for a systematic reassessment of electrostatic interactions in strongly confined media, where highly charged objects polarize an ionic atmosphere, in the presence of multivalent ions, from clay systems and porous media to water structured interfaces in biological context.

METHODS

Simulation: Model, techniques, and parameters

All simulations were done using LAMMPS (http://lammps.sandia.gov) (*56*). We considered a slab geometry that is finite in the z direction and periodic in x and y (the charged surfaces being at $z = 0$ and $z = D$), and we ran separate simulations for each value of the surface charge σ and D. For each set of parameters, exactly 64 calcium counterions were included, and the simulation bounds L_x and L_y were adjusted accordingly to ensure overall charge neutrality. The water is treated explicitly, using the rigid SPC/E model (*57*). Additional simulations with the TIP4P/2005 model (*58*) were performed for three separations. Results on the microscopic correlations and net pressure are shown in section S3.1 and closely match those obtained with the SPC/E model. A more computationally expensive water model, as well as polarizability of water molecules, is not expected to play a key role in simulation results (see section S3.1).

The number of water molecules is set using a GCMC process, discussed in further detail in the next section. To account for the finite size and dispersion interactions of ions, water, and the walls (C-S-H surfaces), we use a Lennard-Jones potential (LJ)

$$U_{\mathrm{LJ}}(r) = 4\epsilon\left[\left(\frac{d}{r}\right)^{12} - \left(\frac{d}{r}\right)^{6}\right] \tag{1}$$

In the SPC/E and TIP4P/2005 models, there is one LJ site per water molecule situated at the oxygen atom. The LJ parameters for the ions are taken from Cygan *et al.* (*59*). The specific values used for the LJ d and ϵ are as follows: $d = 2.87$ Å and $\epsilon = 0.1$ kcal/mol for Ca, $d = 3.17$ Å and $\epsilon = 0.155$ kcal/mol for SPC/E water, and $d = 3.1589$ Å and $\epsilon = 0.162$ kcal/mol for TIP4P/2005 water. Pairs of different types use the arithmetic mean values of d and ϵ. The wall LJ parameters are the same as those of the SPC/E water. This simplified surface interaction does not consider any heterogeneity or roughness of the surface, which might be relevant for other investigations, but our results indicate that these details are not as important for the properties discussed here.

The final ingredient is the Coulomb forces. Calcium ions are treated as having a point charge of $+2e$. The SPC/E and TIP4P/2005 water models have three point charges, two for hydrogen and one for oxygen, although the exact partial charges and their positions vary between the two models. Detailed information can be found in (*57*, *58*). To accurately account for the long-ranged Coulomb forces, we use Ewald summation (*60*). The original formulation is for a 3D periodic system. Yeh and Berkowitz (*61*) showed that treating the 2D periodic slab system as 3D periodic, with some vacuum space inserted between slabs, is accurate given the addition of a geometry-related correction term to the energy. For the slab geometry, this term is

$$E(M, \mathrm{slab}) = \frac{2\pi}{V} M_z^2 \tag{2}$$

where M_z is the z component of the total dipole moment of the simulation cell.

A few comparisons are made to PM simulations with implicit water. These are performed with exactly the same parameters, except that there are no water molecules and, instead, the dielectric constant is set to $\varepsilon_r = 78.0$. Effectively, all electrostatic interactions are screened uniformly instead of letting screening effects arise from rearrangement of discrete water molecules. The resulting disparity is due to the fact that this is an insufficient representation of the effects of water in this system. Comparison is also made with PM calculations in vacuum (i.e., with $\varepsilon_r = 1$); this gives credence to the "locked water" view discussed in the text for the strong coupling regime.

To make direct comparisons with the analytical predictions that use only the dipolar term in the multipole expansion for water, some simulations were performed with purely dipolar interactions for the water molecules [namely, Fig. 5 (A and B) and figs. S5 and S6]. In these cases, the water Coulomb interactions were computed using a point dipole with a moment $m = 0.37\ e$Å $= 1.8$ D selected so that the dielectric constant matches that of water in bulk (room temperature and pressure) conditions.

Water density

Water in confined geometries (especially in the presence of charges) can have a density that is different from bulk conditions. This density is highly dependent on the level of confinement and the strength of the electric fields in the system because of their effect on water structure, so it is a function of D and σ. To select the number of water molecules for our simulations, we first performed GCMC based on the chemical potential of bulk water (room temperature and density). Simulations in bulk conditions showed that a chemical potential of $\mu = -8.8$ kcal/mol gave the correct water density.

This chemical potential can be maintained using the Metropolis method by attempting insertions/deletions with equal probability and accepting them with the following probabilities (*60*)

$$p_{\mathrm{ins}} = \min\left(1, \frac{V}{\Lambda^3(N+1)} e^{\beta(\mu - \Delta U)}\right) \tag{3}$$

$$p_{\mathrm{del}} = \min\left(1, \frac{\Lambda^3 N}{V} e^{-\beta(\mu-\Delta U)}\right) \quad (4)$$

Here, $\beta = 1/(k_B T)$, Λ is the thermal De Broglie wavelength, and ΔU is the internal energy change upon attempting a particle insertion or deletion. Using a Monte Carlo simulation, with random insertions and deletions, the grand canonical ensemble is sampled, and in equilibrium, the chemical potential is maintained with water density fluctuating around a mean value.

The GCMC process alone is very slow to converge to the final density, as it only considers single molecule moves. To speed up the convergence, we combined this with MD, shown previously to significantly decrease the convergence time (*15*), with 1000 GCMC exchanges (insertions and deletions) attempted every 1000 MD steps with a time step of 1 fs. Starting with zero water molecules, the GCMC and MD simulations were run until equilibrium was reached (when energy, pressure, and water density no longer changed with time). With this process, the equilibrium density in confinement was found within 3×10^6 MD steps for the $\sigma = 3e^-/\mathrm{nm}^2$ simulations.

In the low σ simulations (with larger system size), the convergence was found to be very slow because of the larger number of water molecule insertions required. After 3×10^6 MD steps and GCMC exchanges, it remained unclear whether the water density had reached the equilibrium value. In this situation, further simulations were performed using initial configurations with randomly placed water molecules at bulk density ($\rho = 1\ \mathrm{g/cm}^3$). As the initial water density in these configurations was closer to the final one, fewer GCMC exchanges were required to reach an equilibrium value, and this significantly reduced the GCMC simulation time required to converge to the equilibrium density. In addition, we were able to observe convergence toward the final water density from different initial conditions, making it clear that the chosen values were appropriate.

Analysis of pressure and spatiotemporal correlations

After determining the equilibrium number of water molecules for a system with given parameters, we have confirmed that all systems have reached equilibrium by checking that there was no drift in the energy and pressure over time, that time correlations had substantially decayed, and/or that there was no aging sign in two-time correlation functions. We have then generated trajectories in the NVT ensemble using MD and the velocity Verlet algorithm with an integration step of 1 fs. All simulations data discussed here have been averaged over 10^6 MD steps. To ensure sufficient thermodynamic sampling in the cases of high confinement (where dynamics are substantially slower), additional simulations using 10 independent sets of random initial conditions were performed for all samples with $D \leq 12$Å. Both initial ion velocities and the random number seed for the GCMC process were varied, resulting in slight differences in the number of water molecules. In all cases, sample-to-sample fluctuations were smaller than the symbol size in our plots, with a maximal SD in pressure (at $D = 6$ Å) of $s_{\max} < 0.05$ GPa. From the particle trajectories, the pressure and microscopic correlations were computed. The pressure was calculated as the time average of the total force exerted on one of the C-S-H surfaces, which fluctuates around a mean value in equilibrium. This was computed for each value of D, and the pressure profile was obtained from subtracting the large distance ($D = 40$ Å) value of the pressure.

To investigate the microscopic origins of this force, we also study the spatial and dynamical correlations that arise in the ions and water. There are theoretical predictions that ions have strongly correlated positions and may even form 2D crystals [see (*46*) and section S2]. To quantify the extent to which this holds, we calculated the pair correlation function $g(r)$ of ions in the xy plane, i.e., parallel to the C-S-H surfaces, defined as

$$g(r) = \frac{L_x L_y}{2\pi r \Delta r N_{\mathrm{ion}}^2} \left\langle \sum_i \sum_{j \neq i} \mathcal{H}\left(\frac{\Delta r}{2} - |r - r_{ij}|\right) \right\rangle \quad (5)$$

where r_{ij} is the distance between the two ions in the xy plane, Δr is a binning distance, and $\mathcal{H}$ is the Heaviside function. This function was also calculated for specific groups of ions, determined by their z position, which simply involved modifying N_{ion} and the $\sum$ bounds appropriately.

In addition to static spatial correlations, significant dynamical correlations also arise. These have been studied by computing the self-intermediate scattering function (*62*), which quantifies the time correlations of ion (or water molecule) displacements. In particular, we analyzed the dynamics in the direction normal to the surface, z

$$F_s(q_z, t) = \frac{1}{N} \left\langle \sum_{j=1}^{N} e^{\mathrm{i} q_z (z_j(t) - z_j(0))} \right\rangle \quad (6)$$

where the q_z values are determined by the system dimension D and the boundary conditions. The q_z value sets the length scale of displacements that contribute most to $F_s(q_z, t)$, and because of boundary conditions, the lowest allowable value is $q_z = 2\pi/D$. We consider all multiples of this value up to $q_z = 10\ \mathrm{Å}^{-1}$, corresponding to subangstrom length scales. To separate the contributions from different groups of ions or water molecules, we modify the N and the bounds of the $\sum$.

Theory of the electrostatic coupling for high surface charge

A useful and commonly used tool to describe charged solutions at equilibrium, the Poisson-Boltzmann approximation (at the root of the electrostatic contribution to DLVO theory), is a mean-field approach: Ions are treated as a charged cloud, whose density depends on the average electrostatic potential. Spatial correlations between ions and, more generally, discreteness effects are discarded since the charged cloud is viewed as continuum. It can be shown that, within Poisson-Boltzmann theory, the force between two like-charged surfaces is always repulsive (*9*). Accounting for the discrete nature of ions explicitly, attraction may set in under strong enough Coulombic coupling, as we next explain. A fingerprint of the mechanism behind attraction may be found in the xy staggering of ionic patterns between one wall and the other (staggered peaks between the intralayer $g(r)$ and the interlayer $g(r)$, as visible in Fig. 3A).

For a salt-free system such as the one under study here, Poisson-Boltzmann theory is a trustworthy approximation under conditions of weak electrostatic coupling (*13*, *14*). On the other hand, mean-field fails and attraction can take place because of ionic correlations when coupling becomes strong. Electrostatic coupling is quantified through the parameter

$$\Xi = \frac{q^2 l_B}{\mu_{GC}} = 2\pi q^3 l_B^2 \sigma \quad (7)$$

where q is the counterions' valence, σ is the absolute value of the surface charge density of the walls divided by the elementary charge e, $l_B = e^2/(4\pi\varepsilon_0\varepsilon_r k_B T)$ (the Bjerrum length) is the distance between

two elementary charges such that their repulsive potential energy is k_BT, and $\mu_{GC} = (2\pi l_B q\sigma)^{-1}$ (the Gouy-Chapman length) is the distance of a charge qe from the wall such that its attractive potential energy is k_BT. In practice, $q^2 l_B$ quantifies the strength of electrostatic repulsion between counterions, while μ_{GC} quantifies how close to the wall ions tend to stay. When Ξ is small (weak coupling), ions can come relatively close to each other and populate the region within a distance μ_{GC} from the wall without a need to form any ordered structure. Conversely, when Ξ is large (strong coupling), ions lie very close to the walls, but feel a strong mutual repulsion, so they need to form ordered planar structures to minimize their energy.

Ion density and pressure

At strong coupling (the relevant situation here), an ion on either wall is subjected to an effective electric field written for convenience as $\kappa/(\beta q e \mu_{GC}) = \kappa\sigma/(2\varepsilon_0\varepsilon_r)$. The quantity κ can be viewed as the dimensionless local electric field acting onto an ion, with $0 < \kappa < 1$. It depends on wall-wall distance D and stems from electrostatic correlations. For large D, ions that are located in the vicinity of one of the two walls mostly feel the field because of this wall, the other one being screened by the remaining ions: This means $\kappa \simeq 1$. In the opposite limit, when D becomes smaller than the typical ion-ion distance, an ion feels the field created by both walls, in opposite directions, while the contribution due to other ions is subdominant. In this small D regime where all ions essentially lie in the same plane, κ has to vanish. An analytical expression of κ as a function of D has been computed for point-like particles and hard walls in (*14*).

In our simulations, the presence of a soft wall potential does not modify much the picture, except for the fact that D must be replaced by $D_{eff} = D - 2z_c$, where z_c is the equilibrium distance of an n-mer (a Ca ion dressed with n water molecules) from the closest wall. Taking this into account, we find the expression for the effective field given in eq. S14 and plotted in fig. S4B.

The average ion (n-mer) density is then computed as per eq. S15, which can be obtained by deriving the partition function of an ionic system within soft walls, similarly to what is done in (*14*). This is the density that is plotted in Fig. 5 (A and B).

The pressure shown in Fig. 5C is eventually computed from the ion density through eq. S16, which is an extension of the contact theorem, a known exact result. This amounts to splitting the pressure into an electrostatic contribution and a kinetic one, due to interactions with the walls. Before and close to its minimum point, at very small distances, the pressure profile turns out to be dominated by LJ repulsion and can be approximated by eq. S10. After the minimum, the pressure increases in agreement with the analytical hard wall prediction

$$P(D) = 2\pi l_B \sigma^2 k_B T\left[-1 + \kappa(D_{eff})\left(\frac{1 + e^{\kappa(D_{eff})\frac{D_{eff}}{\mu_{GC}}}}{1 - e^{\kappa(D_{eff})\frac{D_{eff}}{\mu_{GC}}}}\right)\right] \quad (8)$$

This is the relevant regime for our study, exhibiting negative P. Note that the pressure prefactor scales as the square of the surface charge and, most importantly, as the inverse of the dielectric permittivity: Within our locked water theory, pressure is enhanced by almost two orders of magnitudes, compared to the PM. More details are given in section S2.2.

Energy of n-mers

The formation of n-mers due to hydration of Ca ions is an energetically driven process for $n < 5$, while entropy comes into play for larger n. The minimum energy of an n-mer was computed (within the dipolar model, more convenient to this end) through a simulated annealing procedure, where an ion was considered fixed next to a wall and energy was minimized with respect to the positions and orientations of n water molecules. Because of the presence of the wall, the volume available to water molecules is restricted to a hemisphere. Considering the minimum energy configuration of an n-mer, the formation energy u_n per n-mer is then refined, accounting for the presence of the (infinitely many) other n-mers, lying in the same plane. Because of the long-range nature of Coulombic interactions, it is important to keep track of all neighbors. u_n turned out to be $\lesssim -50\ n\ k_BT$ for $n \leq 6$ (see Fig. 4C), while $n \geq 7$ was not considered, as the minimum energy configurations are such that no more than six water molecules can fit in one hydration shell. More details are given in section S2.1.

Free energy of n-mers

The free energy $\Delta F_{n \to n+1}$ of formation of an $(n + 1)$–mer, from the absorption of a water molecule on an n-mer, can be assessed using the previously computed values of u_n, the chemical potential μ of bulk water used in simulations, and estimating the associated entropy change. Entropy decreases because of increased confinement of water molecules: This can be quantified by single-particle calculations of the volume available to every water molecule when it is bound to an n-mer, as a function of n. For $n = 3$ and 4, we have $\Delta F_{n \to n+1} < -30\ k_BT$, while $\Delta F_{5 \to 6} \simeq 0$ within a few k_BT. Details can be found in section S2.1. Since adsorbing water molecules to increase n is extremely favorable, at least up to $n = 5$, one can assume all molecules to be bound at strong confinement and predict quantitatively distances D_n at which all ions are bound to exactly n water molecules: We find

$$\rho_w D_n = 2n\frac{\sigma}{q} \quad (9)$$

where $\rho_w D$ is the average number of water molecules per unit surface at distance D.

These simple arguments are in excellent agreement with numerical simulations. Our calculations explain the fraction of bound water (Fig. 4E) observed in simulations as a function of D and the fraction of 5- to 6-mers in simulations with a dipolar approximation for the Coulomb interactions (fig. S6). More details on this limited resources argument are given in section S2.1.

SUPPLEMENTARY MATERIALS

Supplementary material for this article is available at http://advances.sciencemag.org/cgi/content/full/7/32/eabg5882/DC1

REFERENCES AND NOTES

1. International Energy Agency (IEA) for the Global Alliance for Buildings and Construction (GlobalABC), "Global Alliance for Buildings and Construction 2018 Global Status Report," (Technical Report, UN Environment Programme, 2018.
2. G. Habert, S. A. Miller, V. M. John, J. L. Provis, A. Favier, A. Horvath, K. L. Scrivener, Environmental impacts and decarbonization strategies in the cement and concrete industries. *Nat. Rev. Earth Environ.* **1**, 559–573 (2020).
3. A. J. Allen, J. J. Thomas, H. M. Jennings, Composition and density of nanoscale calcium-silicate-hydrate in cement. *Nat. Mater.* **6**, 311–316 (2007).
4. M. J. Abdolhosseini Qomi, K. J. Krakowiak, M. Bauchy, K. L. Stewart, R. Shahsavari, D. Jagannathan, D. B. Brommer, A. Baronnet, M. J. Buehler, S. Yip, F. J. Ulm, K. J. Van Vliet, R. J. Pellenq, Combinatorial molecular optimization of cement hydrates. *Nat. Commun.* **5**, 4960 (2014).
5. K. Ioannidou, K. J. Krakowiak, M. Bauchy, C. G. Hoover, E. Masoero, S. Yip, F.-J. Ulm, P. Levitz, R. J.-M. Pellenq, E. Del Gado, Mesoscale texture of cement hydrates. *Proc. Natl. Acad. Sci.* **113**, 2029–2034 (2016).

6. R. J.-M. Pellenq, H. van Damme, Why does concrete set?: The nature of cohesion forces in hardened cement-based materials. *MRS Bullet.* **29**, 319–323 (2004).
7. C. Plassard, E. Lesniewska, I. Pochard, A. Nonat, Nanoscale experimental investigation of particle interactions at the origin of the cohesion of cement. *Langmuir* **21**, 7263–7270 (2005).
8. A. Gmira, M. Zabat, R. J. Pellenq, H. Van Damme, Microscopic physical basis of the poromechanical behavior of cement-based materials. *Mat. Struct.* **37**, 3–14 (2004).
9. J. Israelachvili, *Intermolecular and Surface Forces* (Academic Press, ed. 3, 2011).
10. Y. S. Jho, R. Brewster, S. A. Safran, P. A. Pincus, Long-range interaction between heterogeneously charged membranes. *Langmuir* **27**, 4439–4446 (2011).
11. W. M. Gelbart, R. F. Bruinsma, P. A. Pincus, V. A. Parsegian, Dna-inspired electrostatics. *Phys. Today* **53**, 38–44 (2000).
12. Y. Levin, Electrostatic correlations: From plasma to biology. *Rep. Prog. Phys.* **65**, 1577–1632 (2002).
13. A. G. Moreira, R. R. Netz, Binding of similarly charged plates with counterions only. *Phys. Rev. Lett.* **87**, 78301 (2001).
14. L. Samaj, M. Trulsson, E. Trizac, Strong-coupling theory of counterions between symmetrically charged walls: From crystal to fluid phases. *Soft Matter* **14**, 4040–4052 (2018).
15. B. Carrier, "Influence of water on the short-term and long-term mechanical properties of swelling clays: Experiments on self-supporting films and molecular simulations," thesis, Universite Paris-Est (2014).
16. S. Masoumi, S. Zare, H. Valipour, M. J. Abdolhosseini Qomi, Effective interactions between calcium-silicate-hydrate nanolayers. *J. Phys. Chem. C* **123**, 4755–4766 (2019).
17. B. Jönsson, H. Wennerström, A. Nonat, B. Cabane, Onset of cohesion in cement paste. *Langmuir* **20**, 6702–6709 (2004).
18. R. J. Pellenq, N. Lequeux, H. van Damme, Engineering the bonding scheme in C–S–H: The iono-covalent framework. *Cem. Concr. Res.* **38**, 159–174 (2008).
19. M. Vandamme, F.-J. Ulm, Nanogranular origin of concrete creep. *Proc. Natl. Acad. Sci.* **106**, 10552–10557 (2009).
20. R. K. Mishra, A. K. Mohamed, D. Geissbühler, H. Manzano, T. Jamil, R. Shahsavari, A. G. Kalinichev, S. Galmarini, L. Tao, H. Heinz, R. Pellenq, A. C. van Duin, S. C. Parker, R. J. Flatt, P. Bowen, *cemff*: A force field database for cementitious materials including validations, applications and opportunities. *Cem. Concr. Res.* **102**, 68–89 (2017).
21. G. Geng, R. J. Myers, M. J. A. Qomi, P. J. Monteiro, Densification of the interlayer spacing governs the nanomechanical properties of calcium-silicate-hydrate. *Sci. Rep.* **7**, 10986 (2017).
22. J. W. Bullard, H. M. Jennings, R. A. Livingston, A. Nonat, G. W. Scherer, J. S. Schweitzer, K. L. Scrivener, J. J. Thomas, Mechanisms of cement hydration. *Cem. Concr. Res.* **41**, 1208–1223 (2011).
23. C. Meral, C. J. Benmore, P. J. Monteiro, The study of disorder and nanocrystallinity in C–S–H, supplementary cementitious materials and geopolymers using pair distribution function analysis. *Cem. Concr. Res.* **41**, 696–710 (2011).
24. C. E. White, L. L. Daemen, M. Hartl, K. Page, Intrinsic differences in atomic ordering of calcium (alumino)silicate hydrates in conventional and alkali-activated cements. *Cem. Concr. Res.* **67**, 66–73 (2015).
25. J. J. Thomas, S. A. FitzGerald, D. A. Neumann, R. A. Livingston, State of water in hydrating tricalcium silicate and portland cement pastes as measured by quasi-elastic neutron scattering. *J. Am. Ceram. Soc.* **84**, 1811–1816 (2001).
26. H. N. Bordallo, L. P. Aldridge, A. Desmedt, Water dynamics in hardened ordinary portland cement paste or concrete: From quasielastic neutron scattering. *J. Phys. Chem. B* **110**, 17966–17976 (2006).
27. A. J. Bohris, U. Goerke, P. J. McDonald, M. Mulheron, B. Newling, B. Le Page, A broad line NMR and MRI study of water and water transport in portland cement pastes. *Magn. Reson. Imaging* **16**, 455–461 (1998).
28. E. Fratini, A. Faraone, F. Ridi, S. H. Chen, P. Baglioni, Hydration water dynamics in tricalcium silicate pastes by time-resolved incoherent elastic neutron scattering. *J. Phys. Chem. C* **117**, 7358–7364 (2013).
29. S. Masoumi, H. Valipour, M. J. Abdolhosseini Qomi, Intermolecular forces between nanolayers of crystalline calcium-silicate-hydrates in aqueous medium. *J. Phys. Chem. C* **121**, 5565–5572 (2017).
30. I. G. Richardson, G. W. Groves, Microstructure and microanalysis of hardened ordinary Portland cement pastes. *J. Mater. Sci.* **28**, 265–277 (1993).
31. B. Lothenbach, A. Nonat, Calcium silicate hydrates: Solid and liquid phase composition. *Cem. Concr. Res.* **78**, 57–70 (2015).
32. W. S. Chiang, E. Fratini, P. Baglioni, D. Liu, S. H. Chen, Microstructure determination of calcium-silicate-hydrate globules by small-angle neutron scattering. *J. Phys. Chem. C* **116**, 5055–5061 (2012).
33. C. Labbez, I. Pochard, B. Jönsson, A. Nonat, C-S-H/solution interface: Experimental and Monte Carlo studies. *Cem. Concr. Res.* **41**, 161–168 (2011).
34. L. B. Skinner, S. R. Chae, C. J. Benmore, H. R. Wenk, P. J. M. Monteiro, Nanostructure of calcium silicate hydrates in cements. *Phys. Rev. Lett.* **104**, 195502 (2010).
35. A. Schlaich, E. W. Knapp, R. R. Netz, Water dielectric effects in planar confinement. *Phys. Rev. Lett.* **117**, 048001 (2016).
36. N. Giovambattista, P. J. Rossky, P. G. Debenedetti, Phase transitions induced by nanoconfinement in liquid water. *Phys. Rev. Lett.* **102**, 050603 (2009).
37. L. Fumagalli, A. Esfandiar, R. Fabregas, S. Hu, P. Ares, A. Janardanan, Q. Yang, B. Radha, T. Taniguchi, K. Watanabe, G. Gomila, K. S. Novoselov, A. K. Geim, Anomalously low dielectric constant of confined water. *Science* **360**, 1339–1342 (2018).
38. S. Koneshan, J. C. Rasaiah, R. M. Lynden-Bell, S. H. Lee, Solvent structure, dynamics, and ion mobility in aqueous solutions at 25 C. *J. Phys. Chem. B* **102**, 4193–4204 (1998).
39. T. Megyes, T. Grósz, T. Radnai, I. Bakó, G. Pálinkás, Solvation of calcium ion in polar solvents: An x-ray diffraction and ab initio study. *J. Phys. Chem. A* **108**, 7261–7271 (2004).
40. D. W. Smith, Ionic hydration enthalpies. *J. Chem. Educ.* **54**, 540–542 (1977).
41. P. M. Claesson, P. Herder, P. Stenius, J. C. Eriksson, R. M. Pashley, An ESCA and AES study of ion-exchange on the basal plane of mica. *J. Colloid Interface Sci.* **109**, 31–39 (1986).
42. X. Shen, I. C. Bourg, Molecular dynamics simulations of the colloidal interaction between smectite clay nanoparticles in liquid water. *J. Colloid Interface Sci.* **584**, 610–621 (2021).
43. K. Ioannidou, R. J.-M. Pellenq, E. Del Gado, Controlling local packing and growth in calcium-silicate-hydrate gels. *Soft Matter* **10**, 1121–1133 (2014).
44. K. Ioannidou, M. Kanduč, L. Li, D. Frenkel, J. Dobnikar, E. Del Gado, The crucial effect of early-stage gelation on the mechanical properties of cement hydrates. *Nat. Commun.* **7**, 12106 (2016).
45. A. Goyal, K. Ioannidou, C. Tiede, P. Levitz, R. J.-M. Pellenq, E. Del Gado, Heterogeneous surface growth and gelation of cement hydrates. *J. Phys. Chem. C* **124**, 15500–15510 (2020).
46. L. Šamaj, E. Trizac, Ground state of classical bilayer Wigner crystals. *EPL* **98**, 36004 (2012).
47. K. L. Scrivener, P. Juilland, P. J. Monteiro, Advances in understanding hydration of Portland cement. *Cem. Concr. Res.* **78**, 38–56 (2015).
48. S. Bishnoi, K. L. Scrivener, Studying nucleation and growth kinetics of alite hydration using μic. *Cem. Concr. Res.* **39**, 849–860 (2009).
49. P. D. Tennis, H. M. Jennings, A model for two types of calcium silicate hydrate in the microstructure of Portland cement pastes. *Cem. Concr. Res.* **30**, 855–863 (2000).
50. K. Ioannidou, E. Del Gado, F.-J. Ulm, R. J.-M. Pellenq, Inhomogeneity in cement hydrates: Linking local packing to local pressure. *J. Nanomech. Micromech.* **7**, 04017003 (2017).
51. M. Abuhaikal, K. Ioannidou, T. Petersen, R. J. Pellenq, F. J. Ulm, Le Châtelier's conjecture: Measurement of colloidal eigenstresses in chemically reactive materials. *J. Mech. Phys. Solids* **112**, 334–344 (2018).
52. T. Zhou, K. Ioannidou, F.-J. Ulm, M. Z. Bazant, R. J.-M. Pellenq, Multiscale poromechanics of wet cement paste. *Proc. Natl. Acad. Sci.* **116**, 10652–10657 (2019).
53. A. Aili, M. Vandamme, J. M. Torrenti, B. Masson, Is long-term autogenous shrinkage a creep phenomenon induced by capillary effects due to self-desiccation? *Cem. Concr. Res.* **108**, 186–200 (2018).
54. H. Van Damme, in *Colloidal Chemo-Mechanics of Cement Hydrates and Smectite Clays: Cohesion vs. Swelling* (Taylor & Francis, 2006), pp. 1411–1426.
55. C. Merlet, B. Rotenberg, P. A. Madden, P. L. Taberna, P. Simon, Y. Gogotsi, M. Salanne, On the molecular origin of supercapacitance in nanoporous carbon electrodes. *Nat. Mater.* **11**, 306–310 (2012).
56. S. Plimpton, Fast parallel algorithms for short-range molecular dynamics. *J. Comput. Phys.* **117**, 1–19 (1995).
57. H. J. C. Berendsen, J. R. Grigera, T. P. Straatsma, The missing term in effective pair potentials. *J. Phys. Chem.* **91**, 6269–6271 (1987).
58. J. L. Abascal, C. Vega, A general purpose model for the condensed phases of water: TIP4P/2005. *J. Chem. Phys.* **123**, 234505 (2005).
59. R. T. Cygan, J.-J. Liang, A. G. Kalinichev, Molecular models of hydroxide, oxyhydroxide, and clay phases and the development of a general force field. *J. Phys. Chem. B.* **108**, 1255–1266 (2004).
60. M. P. Allen and D. J. Tildesley, *Computer Simulation of Liquids* (Oxford Univ. Press, 1987).
61. I.-C. Yeh, M. L. Berkowitz, Ewald summation for systems with slab geometry. *J. Chem. Phys.* **111**, 3155–3162 (1999).
62. J.-P. Hansen, I. McDonald, *Theory of Simple Liquids* (Academic Press, ed. 3, 2006).
63. Y. Zhang, M. Lagi, F. Ridi, E. Fratini, P. Baglioni, E. Mamontov, S. H. Chen, Observation of dynamic crossover and dynamic heterogeneity in hydration water confined in aged cement paste. *J. Phys. Condens. Matter* **20**, 502101 (2008).
64. D. Andelman, Introduction to electrostatics in soft and biological matter, in *Soft Condensed Matter Physics in Molecular and Cell Biology*, W. C. K. Poon, D. Andelman, Eds. (CRC Press, 2006), pp. 97–122.
65. A. G. Moreira, R. R. Netz, Simulations of counterions at charged plates. *Eur. Phys. J. E* **8**, 33–58 (2002).
66. H. Boroudjerdi, Y.-W. Kim, A. Naji, R. R. Netz, X. Schlagberger, A. Serr, Statics and dynamics of strongly charged soft matter. *Phys. Rep.* **416**, 129–199 (2005).
67. G. Goldoni, F. M. Peeters, Stability, dynamical properties, and melting of a classical bilayer wigner crystal. *Phys. Rev. B* **53**, 4591–4603 (1996).

68. E. Trizac, L. Samaj, Like-charge colloidal attraction: A simple argument, in *Proceedings of the International School of Physics Enrico Fermi*, C. Bechinger, F. Sciortino, P. Ziherl, Eds. (IOS, Amsterdam, 2012), vol. 184, pp. 61–73.
69. D. Henderson, L. Blum, J. Lebowitz, An exact formula for the contact value of the density profile of a system of charged hard spheres near a charged wall. *J. Electroanal. Chem.* **102**, 315–319 (1979).
70. P. Mark, L. Nilsson, Structure and dynamics of the TIP3P, SPC, and SPC/E water models at 298 K. *Chem. A Eur. J.* **105**, 9954–9960 (2001).
71. J. Dix, L. Lue, P. Carbone, Why different water models predict different structures under 2D confinement. *J. Comput. Chem.* **39**, 2051–2059 (2018).
72. S. Le Crom, C. Tournassat, J.-C. Robinet, V. Marry, Influence of polarizability on the prediction of the electrical double layer structure in a clay mesopore: A molecular dynamics study. *J. Phys. Chem. C* **124**, 6221–6232 (2020).
73. G. Kamath, S. A. Deshmukh, S. K. Sankaranarayanan, Comparison of select polarizable and non-polarizable water models in predicting solvation dynamics of water confined between MgO slabs. *J. Phys. Condens. Matter* **25**, 305003 (2013).
74. M. Sprik, Hydrogen bonding and the static dielectric constant in liquid water. *J. Chem. Phys.* **95**, 6762–6769 (1991).
75. C. G. Gray, Y. S. Sainger, C. G. Joslin, P. T. Cummings, S. Goldman, Computer simulation of dipolar fluids. Dependence of the dielectric constant on system size: A comparative study of Ewald sum and reaction field approaches. *J. Chem. Phys.* **85**, 1502 (1986).
76. V. A. Froltsov, S. H. L. Klapp, Dielectric response of polar liquids in narrow slit pores. *J. Chem. Phys.* **126**, 114703 (2007).
77. A. Schlaich, A. P. dos Santos, R. R. Netz, Simulations of nanoseparated charged surfaces reveal charge-induced water reorientation and nonadditivity of hydration and mean-field electrostatic repulsion. *Langmuir* **35**, 551–560 (2019).
78. L. Pegado, B. Jönsson, H. Wennerström, Ion-ion correlation attraction in a molecular solvent. *J. Chem. Phys.* **129**, 184503 (2008).
79. E. Schneck, F. Sedlmeier, R. R. Netz, Hydration repulsion between biomembranes results from an interplay of dehydration and depolarization. *Proc. Natl. Acad. Sci.* **109**, 14405–14409 (2012).
80. H. Chen, J. R. Cox, H. Ow, R. Shi, A. Z. Panagiotopoulos, Hydration repulsion between carbohydrate surfaces mediated by temperature and specific ions. *Sci. Rep.* **6**, 28553 (2016).
81. M. D. Jackson, J. Moon, E. Gotti, R. Taylor, S. R. Chae, M. Kunz, A. H. Emwas, C. Meral, P. Guttmann, P. Levitz, H. R. Wenk, P. J. Monteiro, Material and elastic properties of Al-tobermorite in ancient roman seawater concrete. *J. Am. Ceram. Soc.* **96**, 2598–2606 (2013).
82. M. D. Jackson, S. R. Mulcahy, H. Chen, Y. Li, Q. Li, P. Cappelletti, H.-R. Wenk, Phillipsite and Al-tobermorite mineral cements produced through low-temperature water-rock reactions in Roman marine concrete. *Am. Mineral.* **102**, 1435–1450 (2017).
83. J. P. Oleson, C. Brandon, S. M. Cramer, R. Cucitore, E. Gotti, R. L. Hohlfelder, The ROMACONS project: A contribution to the historical and engineering analysis of hydraulic concrete in Roman maritime structures. *Int. J. Nautical Archaeol.* **33**, 199–229 (2004).
84. D. Moore, *The Roman Pantheon: The Triumph of Concrete* (MARC/CCEOP, University of Guam Station, 2010).
85. R. Courland, *Concrete planet: The strange and Fascinating story of the World's Most Common Man-Made Material* (Prometheus Books, 2011).
86. C. Simonnet, *Le béton: Histoire d'un Matériau: Économie, Technique, Architecture* (Parenthèses, 2005).

Acknowledgments

Funding: This work has received funding from the European Union's Horizon 2020 research and innovation programme under Marie Skłodowska-Curie grant agreement 674979-NANOTRANS. A.G. and E.D.G. acknowledge the NIST PREP Gaithersburg Program (70NANB18H151) and Georgetown University for support. **Author contributions:** A.G. performed all numerical simulations and data analysis. I.P. performed the analytical calculations. R.J.-M.P., E.T., and E.D.G. designed the research. All authors provided critical feedback, helped shape the research and analysis, and wrote the manuscript. **Competing interests:** The authors declare that they have no competing interests. **Data and materials availability:** All data needed to evaluate the conclusions in the paper are present in the paper and/or the Supplementary Materials. Additional data related to this paper may be requested from the authors.

Submitted 15 January 2021
Accepted 17 June 2021
Published 4 August 2021
10.1126/sciadv.abg5882

Citation: A. Goyal, I. Palaia, K. Ioannidou, F.-J. Ulm, H. van Damme, R. J.-M. Pellenq, E. Trizac, E. Del Gado, The physics of cement cohesion. *Sci. Adv.* **7**, eabg5882 (2021).

Science Advances

The physics of cement cohesion

Abhay Goyal, Ivan Palaia, Katerina Ioannidou, Franz-Josef Ulm, Henri van Damme, Roland J.-M. Pellenq, Emmanuel Trizac and Emanuela Del Gado

Sci Adv **7** (32), eabg5882.
DOI: 10.1126/sciadv.abg5882